Atmos. Meas. Tech. Discuss., 4, 247–284, 2011
www.atmos-meas-tech-discuss.net/4/247/2011/
doi:10.5194/amtd-4-247-2011

Atmospheric Measurement Techniques Discussions

Development and characterization of the CU ground MAX-DOAS instrument: lowering RMS noise and first measurements of BrO, IO, and CHOCHO near Pensacola, FL

S. Coburn[1], **B. Dix**[1], **R. Sinreich**[1], **and R. Volkamer**[1,2]

[1]Department of Chemistry and Biochemistry, University of Colorado, Boulder, CO, USA
[2]CIRES – Cooperative Institute for Research in Environmental Sciences, Boulder, CO, USA

Received: 11 November 2010 – Accepted: 4 January 2011 – Published: 17 January 2011

Correspondence to: R. Volkamer (rainer.volkamer@colorado.edu)

Published by Copernicus Publications on behalf of the European Geosciences Union.

Abstract

We designed and assembled the University of Colorado Ground Multi AXis Differential Optical Absorption Spectroscopy (CU GMAX-DOAS) instrument to retrieve bromine oxide (BrO), iodine oxide (IO), formaldehyde (HCHO), glyoxal (CHOCHO), nitrogen dioxide (NO_2) and the oxygen dimer O_4 in the coastal atmosphere of the Gulf of Mexico. The detection sensitivity of DOAS measurements is directly proportional to the root mean square (RMS) of the residual spectrum that remains after all absorbers have been subtracted. Here we describe the CU GMAX-DOAS instrument and demonstrate that the hardware is capable of attaining RMS values of $\sim 6 \times 10^{-6}$ without apparent limitations other than photon shot noise.

Laboratory tests revealed two factors that, in practice, limit the RMS: (1) detector non-linearity noise, RMS_{NLin}, and (2) temperature fluctuations that cause variations in optical resolution (full width at half the maximum, FWHM, of atomic emission lines) and give rise to optical resolution noise, RMS_{FWHM}. The non-linearity of our detector is low ($\sim 10^{-3}$) yet – unless actively controlled – is sufficiently large to create a RMS_{NLin} limit of up to 1.4×10^{-4}. The optical resolution is sensitive to temperature changes (0.03 detector pixels/°C at 334 nm), and temperature variations of 0.1 °C can cause residual RMS_{FWHM} of $\sim 1 \times 10^{-4}$. Both factors were actively addressed in the design of the CU GMAX-DOAS instrument.

The CU GMAX-DOAS was set up at a coastal site near Pensacola, FL, where we detected BrO, IO and CHOCHO in the marine boundary layer (MBL), with daytime average tropospheric vertical column densities, VCDs, of $\sim 2 \times 10^{13}$ molec cm^{-2}, 8×10^{12} molec cm^{-2} and 4×10^{14} molec cm^{-2}, respectively. HCHO and NO_2 were also detected with typical MBL VCDs of 1×10^{16} and 3×10^{15}. These are the first measurements of BrO, IO and CHOCHO over the Gulf of Mexico. The atmospheric implications of these observations for elevated mercury wet deposition rates in this area are briefly discussed. The CU GMAX-DOAS has great potential to investigate RMS-limited problems, like the abundance and variability of trace gases in the MBL and possibly the free troposphere (FT).

AMTD
4, 247–284, 2011

1 Introduction

Tropospheric halogen species, such as bromine oxide (BrO) and iodine oxide (IO), are of great interest to the emerging debate over the inter-relationships between air quality and climate change since they can destroy tropospheric ozone (O_3), which is both toxic and a greenhouse gas; can affect the partition of Nitrogen Oxides (NO_x) and Hydrogen Oxides (HO_x); may play a role in oxidizing gaseous elemental mercury (GEM, Hg^0) to gaseous oxidized mercury (GOM, Hg^{2+}); and, for IO, can form new particles and/or add to the growth of pre-existing particles that may have adverse health effects and can have the potential to cool climate. The detection of halogen oxides, in particular BrO, can pose experimental challenges. For instance, the detection of tropospheric BrO is very difficult due to its relatively low concentrations and its background abundance in the stratosphere. Whereas BrO radicals are typically about ten times as abundant as bromine atoms, both species are in a rapid photochemical steady state. BrO and bromine atoms are very reactive, and are rapidly lost by reaction with oxygenated volatile organic compounds (OVOCs), such as formaldehyde (HCHO) and glyoxal (CHOCHO), HO_2 radicals, NO_x, or heterogeneous reactions, e.g. on surfaces, or in sampling lines. This leads to considerable analytical challenges with the sampling of these free radicals from the atmosphere by means of in-situ techniques and results in horizontal and vertical distributions of reactive bromine radicals that are very susceptible to gradients in the concentrations of OVOCs, HO_2, and NO_x. The dependence on reactant gradients poses the question of how representative measurements near ground-level are over the depth of the marine boundary layer (MBL) and throughout the atmosphere. One way to investigate abundance of reactive halogen species is by detecting halogen oxide radicals directly in the open atmosphere using Differential Optical Absorption Spectroscopy (DOAS).

DOAS is a well-established technique (Platt and Perner, 1980; Platt, 1994; Platt and Stutz, 2008) used to identify trace gases by means of their individual differential (i.e. narrow band) absorption structures. In the past, the DOAS technique has been

AMTD
4, 247–284, 2011

extensively used to measure halogen oxides (Hönninger et al., 2004; Wagner et al., 2007). Multi-AXis DOAS (MAX-DOAS) is a useful analytical technique that uses scattered sunlight collected at different viewing angles relative to the horizon to measure atmospheric trace gases directly in the open atmosphere (without the need to draw air through any sampling lines). The integrated concentrations of trace gases along each line of sight, termed the Slant Column Density (SCD), is derived using non-linear least-square fitting of multiple trace gas reference spectra. Each spectrum is analyzed against a user-defined reference spectrum, which removes Fraunhofer absorption lines. The reference spectrum is usually recorded in the zenith viewing direction and at a low solar zenith angle (SZA) in order to remove the influence of stratospheric absorbers and the contribution of the reference SCD. This produces a so called differential slant column density (dSCD). If the instrument is ground-based and the telescope is pointed close to the horizon, the increased path length through the surface layer of the atmosphere makes this technique particularly sensitive to trace gases within the boundary layer (Hönninger and Platt, 2002; Hönninger et al., 2004). This creates a distinct advantage in the use of MAX-DOAS to probe the marine/coastal boundary layer.

In the DOAS analysis, the residual structure of the fitting procedure is an indicator for the quality of the fit. This is usually expressed by the root mean square (RMS) of the residual's optical density. RMS of state-of-the-art hardware is typically limited to $\sim 1 \times 10^{-4}$ or higher, i.e., it does not improve further in accordance with photon-count statistics. The reasons for this have, to our knowledge, as yet not been elucidated. There are several parameters that influence the RMS: e.g. omitting relevant cross-sections in the fitting process is alerted by higher (less suitable) RMS; the quality of the reference spectra used during analysis; the analysis parameters; conditions while acquiring the spectra; or the instrumentation. In particular, the choice of the instrumentation used for the measurement can inherently determine the RMS when acquiring the spectra. Imaging spectrometers with longer focal lengths provide more steady projecting properties; larger size array detectors, and larger slit sizes provide for increased

AMTD
4, 247–284, 2011

light throughput and thus lower photon shot noise, while smaller spectrometer/detector combinations tend to be more sensitive to temperature variations and optical drift. In part because larger focal length spectrometers and larger detector arrays are disproportionally more expensive, the advantages of small practical devices have recently been driving the development of MAX-DOAS hardware; one example of this is the Mini-MAX-DOAS hardware (Hönninger, 2002). Mini-MAX-DOAS devices can be easily operated at remote sites, such as volcanoes (e.g., Bobrowski et al., 2003), with just battery power, or be set up quickly at any site, such as on vehicles (e.g., Ibrahim et al., 2010). However, currently available Mini-MAX-DOAS devices are often limited to RMS $\sim 10^{-3}$. In order to detect low concentrations of halogen oxide radicals more sophisticated devices are desirable. State-of-the-art DOAS hardware provides for RMS on the order of 10^{-4}. Recently, the first measurements with RMS values in the range of 8×10^{-5} have been reported (Frieß et al., 2010) with a very stable instrument in the pristine Antarctic environment. Table 1 lists selected typical MAX-DOAS instruments and a few of their respective properties, including their RMS values. The limitations on the attainable RMS values are one of the driving forces preventing the routine measurement of BrO by means of MAX-DOAS. A BrO dSCD on the order of 1×10^{13} molec cm^{-2} corresponds to a differential optical density of 8×10^{-5}; however, even lower dSCD values would still be atmospherically relevant for oxidizing mercury, and/or could affect the tropospheric ozone background. Consequently, low RMS measurements ($<10^{-4}$) are a prerequisite to advancing our understanding of the bromine content of the atmosphere. In order to detect the low optical densities characteristic of BrO column abundances, improvements in the RMS values are a limiting factor.

Measurements by the Mercury Deposition Network (MDN) show that the southeastern United States is a region with elevated mercury wet deposition compared with the rest of the country. This cannot be solely attributed to mercury sources to the atmosphere, which are more abundant in other areas, such as the North Eastern United States industrial corridor, or natural sources that are more dispersed. This discrepancy suggests that the high deposition of mercury to the southeast might be due to the

AMTD
4, 247–284, 2011

conversion of background atmospheric GEM to GOM, the latter of which is then readily wet-deposited. Whether this process would occur in the boundary layer, in the free troposphere (FT), and/or is a combination of both processes, remains unknown. Only small concentrations of bromine atoms (corresponding to <2 ppt of BrO) are sufficient to account for the observed levels of GOM (Holmes et al., 2009).

The ATMOSpeclab at the University of Colorado at Boulder (CU) has developed and characterized a high sensitivity Ground-based MAX-DOAS instrument, the CU GMAX-DOAS. Here we describe the instrument, and present, to our knowledge, the first systematic study of the factors limiting RMS values as the photon shot noise contribution is reduced to $RMS_{PSN}<10^{-4}$. We also present a first application of the CU GMAX-DOAS instrument to measuring BrO, IO, HCHO, CHOCHO, NO_2 and O_4 at a coastal site near Pensacola, FL. This coastal site is in close proximity to a MDN station, and the Gulf of Mexico. The CU GMAX-DOAS was developed to investigate the potential role of halogens in mercury oxidation by measuring the relative abundances and vertical distributions of both BrO and IO.

2 Instrument description

The CU GMAX-DOAS instrument collects spectra of scattered sunlight between 321.3 and 488.4 nm at different viewing angles, which are then analyzed in order to detect the presence of BrO, HCHO, IO, CHOCHO, NO_2, and O_4. The instrument consists of a telescope, located outdoors on an elevated platform to collect scattered sunlight, and the spectrometer/electronics rack, which is kept indoors in an air-conditioned lab and has a two stage temperature control; it contains all of the electrical components needed to operate the instrument, as well as the spectrometer and detector. Figure 1 depicts the instrument components along with their placement and a map of the field sites at which it has been located. When comparing different MAX-DOAS hardware (Table 1), the effective slit area, which is the product of the height over which the detector is

AMTD
4, 247–284, 2011

used and slit width, is a measure of the instrument's ability to couple in-coming light onto the detector; in this regard, the CU GMAX-DOAS is one of the most light-efficient instruments.

2.1 Telescope

The telescope is designed for high light throughput and very low dispersion (cone angle of 0.3°). It is comprised of the motor housing, the rotating prism housing with prism, and the lens tube. The outer components are made from black anodized aluminum and are protected by a thin polished aluminum shield in order to reduce solar heating of the telescope (Fig. 1b,c). The rotating prism housing is driven by an Intelligent Motion Systems Inc. MDrive34 Plus motor (48 V, 4 A maximum) located in the motor housing. The shaft of the motor is attached directly to a custom-made rotating assembly that holds a 5 cm × 5 cm right angle fused silica prism; and a O-ring sealed sapphire window (optical diameter 50.8 mm). During measurement, light is collected via the sapphire window on the main face of the prism housing and enters the prism where it is directed onto an $f/4$ 5 cm lens mounted in the opposite direction from the motor onto the prism holder. Both junctions of the prism housing contain two separate O-ring seals to prevent water from entering the prism housing. Additionally, both the prism housing and the lens tube contain small bags filled with silica gel bead drying agent to actively dry the air around the optics and prevent possible condensation on the optical components. The entire prism housing can be rotated 360° by changing the motor axis; this rotation defines the elevation angle over which the prism collects light from the atmosphere. The telescope and electronics rack are coupled by optical fibers and electronics cables. The light is focused via the lens tube onto a CeramOptics 10 m × 1.7 mm silica monofiber that is connected to an OceanOptics 5 m fiber bundle consisting of 27 × 200 µm fibers. This fiber bundle is configured in a circular arrangement at the fiber junction and then forms a linear array at the spectrometer end. This end of the fiber bundle is directed onto the slit of the spectrometer, which is set at a width of 110 µm. Two filters; a BG3 and a BG38, were placed inside the lens tube just prior to the monofiber to reduce

AMTD
4, 247–284, 2011

the amount of light outside the measured wavelength range that could contribute to stray-light in the spectrometer, as well as to balance out the light intensity differences between the UV and visible wavelength regions across the detector. The chosen optics maximizes the amount of light collected, thus improving the signal-to-noise ratio and time resolution of measurements.

2.2 Spectrometer, CCD detector and electronics rack

The rack containing the spectrometer and controlling electronics is comprised of a standard 19″ aluminum instrument rack with modifications to the floor and the lid. The spectrometer is a Princeton Instrument Acton SP2356i Imaging Czerny-Turner spectrometer with a PIXIS 400 back illuminated CCD detector. The spectrometer was equipped with a custom 500 grooves mm^{-1} grating (Richardson, 300 nm blaze angle). This grating gives simultaneous coverage from 321.3–488.4 nm, or a range of 167.1 nm. The quadratic dispersion equation for this grating is

$$\lambda = 321.2700 + 0.1252(x) - 2.6559 \times 10^{-7}(x^2) \quad (1)$$

where x denotes the pixel number, and the linearly approximated dispersion is 0.125 nm $pixel^{-1}$. The 110 µm wide slit width corresponds to a linearly approximated spectral resolution of ~0.68 nm FWHM. This has been experimentally determined by means of fitting a Gaussian function to a mercury atomic line spectrum of the 404.66 nm line to be ~0.74 nm. The PIXIS 400B CCD is a UV-optimized two-dimensional array detector with 400 × 1340 pixels. Our software sets the gain of the readout register ADC during CCD initialization. This CCD gain is typically set to the lowest gain value (high capacity mode), which corresponds to a photon-into-count conversion factor of 16; increasing this gain makes the CCD more sensitive (values of 1<conversion factor<16 are accessible) but also reduces the pixel well capacity, and thus has the primary effect to shorten integration times to reach a certain saturation level. Notably, the use of the CCD in high capacity mode maximizes the useful well capacity, and minimizes the attainable RMS noise from a single acquisition. For CCD

AMTD
4, 247–284, 2011

readout, two rows are binned to reduce data volume; we use a readout rate of 2 MHz (readout noise<16 electrons rms), corresponding to a readout time of 134 ms. The CCD is cooled to −70 °C to reduce dark current. It was verified in laboratory tests that electronic noise and dark current noise are negligible, and RMS noise essentially follows photon counting statistics. The data acquisition software reads a configuration file that specifies a lower and upper row number for illuminated CCD rows (ROI or "region of interest"), and similarly specifies row numbers for "dark" areas of the CCD chip; the latter are used to characterize background in terms of electronic offset, dark current, background and spectrometer straylight. The software saves both a background corrected 1-D spectrum, and a full 2-D image. For instrument control, a National Instruments CompactRIO electronics chassis, capacity of up to eight modules, was interfaced with a custom built Labview data acquisition code to provide a framework for tracking and controlling numerous instrument parameters, including voltage monitoring, temperature read-back, solid state relay control for software PID temperature stabilization, and communications with the telescope motor, spectrometer and CCD detector.

Temperature stability is a key component to consider when designing and building MAX-DOAS instrumentation because even small fluctuations can result in changes in instrument properties, such as line shape and dispersion of the spectrometer, and dark current noise in the detector. In order to maintain a stable temperature, the spectrometer was fitted with insulating foam and a small heating foil controlled by a PID loop in the LabVIEW software. Two temperature sensors were placed on the instrument, one on the bottom near the heating foil to provide feedback for the PID loop and one on the top of the instrument to provide information about the temperature gradient over the spectrometer chassis. Additionally, the rack was fitted with an external housing that provided insulation between the inside of the rack and the ambient air. The top of this housing was equipped with 6 single-stage peltier cooling units, used to stabilize the temperature inside the rack. The peltiers are controlled by a series of heavy duty solid state relays that are triggered by a signal received from a PID controlled solid

AMTD
4, 247–284, 2011

state relay inside the instrument rack. With these measures in place, during normal operation, the sensor closest to the heating foil demonstrated constant temperature to within 0.005 °C, while the sensor atop the instrument showed variability within 0.06 °C over an 8 h period. During this time the rack temperature was stable to within ~0.8 °C while ambient temperature varied by more than 6 °C.

3 Laboratory characterization of the CU GMAX-DOAS

The entire instrument is controlled through custom-built LabVIEW software with a PC interface, allowing configuration and further optimization of the parameters needed to increase the measurement sensitivity to atmospheric trace gases. These parameters include selecting and controlling the CCD target saturation level (which represents the percentage number of the dynamic range of the 16-bit ADC used to digitize the spectrum), setting bounds to the target saturation level, automatic determination of the proper integration time based on the chosen saturation level, automatic rejection of saturated spectra prior to the data storage, and fine tuning the PID parameters used for temperature stabilization of the electronics rack housing as well as the spectrometer.

Prior to deployment, the instrument was characterized in a series of laboratory experiments assessing spectral drift in the wavelength-pixel mapping, changes in the slit function as a function of temperature, optical resolution across the detector, and signal-to-noise levels.

3.1 Temperature sensitivity tests

To test the temperature sensitivity of the instrument, atomic line spectra from a PenRay Mercury-Argon lamp were recorded at five different temperatures ranging from 27 °C to 40 °C. The lines at 334.15 nm (~pixel 104), 404.66 nm (~pixel 667), and 435.84 nm (~pixel 918) were chosen to characterize the shifts (changes in the line center position) and changes in line shape over this temperature range in the center position of

AMTD
4, 247–284, 2011

the CCD detector (404 nm line) and off-center of the CCD detector. These tests were performed by first allowing the spectrometer to stabilize for ~1 h at the desired temperature and then recording the line spectra using the Hg-Ar lamp. These spectra were then analyzed by fitting a Gaussian line shape profile to each of the atomic lines (IgorPro, Wavemetrics). The center position and line width parameters derived from the fitting procedure were used to determine both shifts and line broadening as a function of temperature (Fig. 2). Shift is defined as the difference in the center position of the fit for each temperature; line width broadening is the difference in the FWHM derived from the fit as compared to a reference FWHM. Drift in the wavelength pixel mapping (shift) of this instrument is ~1 pixel for every 10 °C, or ~0.1 pixel °C^{-1}. The dependence of shift on temperature is found to be well-represented by a linear regression (Fig. 2d). The linear regression coefficients were determined to be 0.08 ± 0.01 pixels °C^{-1}, for the three slopes in Fig. 2d, and the offsets were -2.43 ± 0.36 pixels, -2.36 ± 0.35 pixels, -2.36 ± 0.34 pixels, with R^2 values of 0.95 for the three lines, respectively.

3.2 Effect of line-shape broadening on RMS

Table 2 illustrates the effect of line shape broadening on the RMS values obtainable during a DOAS fitting procedure. The effect of line shape broadening was determined by convoluting a literature Fraunhofer spectrum (Kurucz et al., 1984) with Gaussian shaped calculated line-shape functions that differed in FWHM by the number of pixels as given in Table 2. The convoluted Fraunhofer spectrum was then divided by a Fraunhofer spectrum convoluted using a reference line shape width (here 0.79 nm). These tests were conducted in two wavelength ranges as illustrated in Table 2. If combined with the uncertainty in our current temperature stabilization, the attainable RMS range from $<5 \times 10^{-5}$ to 1.5×10^{-4}, with larger numbers expected in the UV region of the spectrum. Since the slit temperature is somewhat buffered by the heat capacity of the spectrometer, its stability could be nearer to the lower limit of these bounds.

AMTD
4, 247–284, 2011

3.3 Shift characterization

The numerical uncertainty with which different reference spectra can be mapped onto a common wavelength pixel relation during the non-linear least square analysis of DOAS spectra depends on the absolute accuracy of the wavelength calibration of literature cross-sections. In order to assess the effect of shift error on the RMS, identical spectra were systematically shifted by the amounts shown in Table 3 and then divided. The shift error effect on RMS was determined to be independent of number of photons of the spectrum. The wavelength regions between 430–470 nm and 330–370 nm were used, which corresponds to 323 and 320 pixels, respectively. Table 3 shows that in order to achieve an RMS on the order of 1×10^{-4} and 1×10^{-5} the shift accuracy needs to be determined to $\sim 6 \times 10^{-3}$ and $\sim 6 \times 10^{-4}$ pixels for the visible region, and $\sim 4 \times 10^{-3}$ and $\sim 4 \times 10^{-4}$ pixels in the UV spectral range. Notably, the uncertainty in the wavelength calibration of literature cross-sections can become limiting if such low RMS is to be realized. The highest wavelength precision is typically achieved by recording laboratory cross-sections using a Fourier Transform Spectrometer (FTS). Notably, the wavelength inaccuracy of an FTS is about $0.05\,\mathrm{cm}^{-1}$, unless special precautions are taken to cross-calibrate wavelength against absolute wavelength standards before and after each spectrometer configuration/beamsplitter change while recording the absorption cross-section spectra in the laboratory. At 450 nm, or $22\,222\,\mathrm{cm}^{-1}$, this translates into 0.001 nm uncertainty in the wavelength calibration of the FTS recorded absorption cross-section spectrum, slightly less at shorter wavelengths. At a typical dispersion of spectrometers used in MAX-DOAS applications (0.1 nm/pixel), this corresponds to an uncertainty in the wavelength pixel mapping of the convoluted reference spectrum of ~0.01 pixels at 450 nm, and about ~0.006 pixels at 350 nm. If strong absorbers like Fraunhofer lines and NO_2 are forced onto identical wavelength pixel mappings for the purpose of least-square fitting procedures that are typically used to determine shifts, this uncertainty in the wavelength pixel mapping of ~0.01 pixels is of the same magnitude as other error sources, and can become a limiting quantity in the RMS noise range below $\sim 10^{-4}$.

AMTD
4, 247–284, 2011

3.4 Detector non-linearity

A sequence of laboratory experiments revealed the non-linearity of the detector as a critical property with applications that use solar stray-light (Fig. 3). These tests were comprised of taking zenith and low elevation angle spectra at varying detector saturation levels and testing the effect of analyzing the low elevation angle spectra using either a zenith spectrum of the same saturation level or one of a different saturation level.

The DOAS retrieval program, WinDOAS (Fayt and Roozendael, 2001), was used to process spectra from these and all subsequent tests. The software performs a non-linear least-squares fit by simultaneously adjusting the optical cross-sections of relevant atmospheric trace gases in the respective wavelength range to the measured spectra. To account for broad band effects (in particular caused by Rayleigh and Mie-scattering) a third degree polynomial was included. The fitting procedure is performed with the logarithm of the spectra (i.e. in optical density space). Additionally, the software can accommodate shifting the analyzed spectra in order to account for spectrometer drifts, which result in differences in the wavelength pixel mapping between the reference and the analyzed spectrum. In some cases a pre-logarithmic linear intensity offset was included to account for stray-light. All of these parameters are adjustable via the software interface and can be optimized for different retrievals, such as the tests described here. Analyzing spectra recorded at different saturation levels can cause $(1-\sigma)$ optical density residual structures in a range from 3×10^{-5} to 1.8×10^{-4} in the UV and from 2×10^{-5} to 7×10^{-5} for the visible wavelength range. The increase in RMS is found to depend (linearly) on the difference in saturation levels between the two spectra (Fig. 3).

The limitation in RMS is caused by the shape of Fraunhofer lines and depends on the saturation level at which spectra are recorded (Figs. 3 and 4). Fit results for spectra with $N=10^{10}$ photons are compared in Fig. 4. When analyzing a spectrum using a reference recorded at the same saturation level the RMS noise is within 10% of the

AMTD
4, 247–284, 2011

theoretical noise, and including an offset in the fit has virtually no effect on the attainable RMS noise level (Fig. 4 top row). However, when a spectrum is analyzed using a reference recorded at a different saturation level, in this case 10% and 90%, the RMS noise is five times higher than the theoretical noise, and including an offset in the fit has a pronounced effect in (artificially) lowering the RMS noise level by about a factor of two (Fig. 4 bottom row). Moreover, the spectral shape of the fitted offset spectrum is strongly anti-correlated with the Ring spectrum, and including the offset spectrum has a strong effect on the value of the Ring fit coefficient. Regardless of the fact that a small Ring fit-coefficient is expected, i.e., spectra recorded within few 10 min at constant elevation angle and mostly clear sky, the ring fit coefficient is more than 10 times greater and of opposite sign if the spectra are recorded at different saturation levels. The demonstrated increase in RMS cannot be explained by atmospheric absorbers, which are accounted for in the analysis procedure, and is a strong indication that nonlinearities in the detector limit the way that Fraunhofer lines can be characterized with available state-of-the-art CCD detectors.

Figure 4 also demonstrates that the distortion of Fraunhofer lines from detector nonlinearity is not necessarily a problem that limits DOAS RMS. Only an inconsistent use of the detector causes a limitation, due to the inconsistent characterization of Fraunhofer lines, and gives rise to RMS_{NLin} to limit the overall RMS. In order to reduce RMS_{NLin} to $<2 \times 10^{-5}$, the saturation level of the detector cannot vary by more than 30% at 440 nm, and not more than 10% at 350 nm (Fig. 3). The solution implemented in the ATMOSpeclab data acquisition LabVIEW code is that in addition to a given target saturation level two additional variables are set, i.e., the upper and lower limit for the target saturation. These provide not-to-exceed bounds to the target saturation during the acquisition of spectra. Prior to the acquisition of each spectrum, a test spectrum is recorded, and the light intensity of this test scan is used to set the integration time of the spectrum in such a way that the detector is used within narrow bounds of the target saturation. This approach was first presented by Volkamer et al. (2009) and is implemented here in the first field deployment of the CU GMAX-DOAS instrument.

AMTD
4, 247–284, 2011

4 Characterization at field site

The CU GMAX-DOAS instrument was deployed at two different field sites in the coastal panhandle of Florida during 2009–2010 (Fig. 1d). It operated at the first site, the South Eastern Aerosol Research (SEARCH) network site Operation Landing Field #7 (OLF) (Hansen et al., 2003), from March to May 2009. The current measurement site is a US Environmental Protection Agency (EPA) facility in Gulf Breeze, FL (∼10 km southeast of Pensacola, FL). The EPA site is located ∼1 km from the ocean and there is a large bay area ∼4 km to the north. The instrument has been operating at this site for the time periods May–September 2009, March–May 2010, and since July 2010.

4.1 Signal-to-noise tests

The signal-to-noise as a function of the number of photons collected was characterized using our LabVIEW-based processing tool called the Intelligent Averaging Module (IAM). Scattered sunlight spectra were collected in two modes of operation: (1) during normal measurements, where a set of eleven different elevation angles each with an integration time of 30 s were scanned during one measurement sequence, and (2) during a viewing routine that measured only two elevation angles; 80° (which served as the reference) and 25°, and twenty spectra were taken sequentially at both elevation angles all with 5 s integration times.

Unless otherwise noted, the WinDOAS settings for all tests included two wavelength regions, between 340–359 nm where BrO is measured and 425–438 nm where IO is measured. The fitted cross-sections included in both wavelength regions were: two O_3 cross-section references (T =223 K and 243 K) (Bogumil et al., 2003), two NO_2 cross-section references (T =220 K and 294 K) (Vandaele et al., 1997), an O_4 cross-section reference (Hermans, 2002), and a Ring reference spectrum. The Ring reference was calculated using the DOASIS software (Kraus, 2006) from a spectrum measured with our instrument. Additionally, in the visible region an IO (Hönninger, 1999) cross-section reference and a water vapour cross-section reference (Rothman et al., 2005) were

AMTD
4, 247–284, 2011

included, and in the UV region a BrO (Wilmouth et al., 1999) cross-section reference and an HCHO (Meller and Moortgat, 2000) cross-section reference were included. In the analysis of the set of data collected during normal operations, a routine was used such that each spectrum was analyzed by a close in time reference spectrum; this helped to accurately characterize and eliminate stratospheric absorbers. In this case, only one NO_2 (T=294 K) cross-section reference and one O_3 (T=223 K) cross-section reference were used. For the routine using only two viewing angles, IAM was used in two different ways to process these spectra. The first use included adding a specified number of spectra for the viewing angles and then analyzing the resulting spectrum. In the second method, ratios were created using two sequential spectra of the same viewing angle, and these ratios were then added together to form the final spectrum that was used in the analysis. In the first method, 4, 16, and 64 spectra were added together before running the analysis. For the second method, the wavelength region between 415–440 nm was used and the IO cross-section omitted and instead a CHOCHO cross-section reference (Volkamer et al., 2005) was included. The ratios were created using sequential spectra and then final spectra were made of the sum of 500 and 1000 ratio spectra. IAM has the capability to shift spectra before and during processing through the use of a shift input file, but for this study only unshifted spectra were used in IAM. For the processing of the spectra created by the first method used by IAM, both NO_2 and O_3 cross-section references were fitted, and the reference spectrum was created by IAM from adding 20 sequential individual 80° spectra (this summed spectrum was then used to calculate the Ring reference spectrum). For the spectra created using the second IAM method, no reference was used, the Ring was the same that was used for the first method, and no offset was included. The results from these tests along with the theoretical noise, based on photon counting statistics, are summarized in Fig. 5. Theoretical noise based on photon counting statistics was calculated according to the equation

$$\mathrm{RMS} = \left(\left(1/N_{\mathrm{ms}}\right)^2 + \left(1/N_{\mathrm{rs}}\right)^2 \right)^{1/2} \quad (2)$$

AMTD
4, 247–284, 2011

where N_{ms}=the number of photons in the measured spectrum and N_{rs}=the number of photons in the reference spectrum. By increasing the numbers of photons collected we achieved RMS values as low as $\sim 1 \times 10^{-5}$ and $\sim 6 \times 10^{-6}$ in the UV and visible regions, respectively. Such low RMS requires acquisition of $>10^{10}$ photons, and demonstrates the reasoning for building a light-efficient instrument (Fig. 5). Figure 6 demonstrates that incorporating high light-throughput optics is key to realize such low RMS in our setup: here data from a single day was analyzed using reference spectra that differed by a fixed time difference, Δt, to the analyzed data. For Δt values of 5, 240, 900, 3600 and 18 000 s were chosen. As Δt is increased beyond few 10 min, the RMS is observed to increase. These results are also summarized in Table 4, showing that using spectra taken close in time generally results in lower RMS values, even though the same number of photons are accumulated.

The effect of detector non-linearity has been actively suppressed in these tests by controlling the target saturation level within narrow bounds. However, the temperature of the slit is expected to vary on a time scale at which heat fluxes equilibrate in our system (few 10 min), and the results in Fig. 6 are generally consistent with variations in the line shape broadening (see Sect. 3.2, Table 2). We conclude that the effect of line shape broadening is most likely to explain the empirical observation of increasing RMS with increasing time difference between two spectra (Table 4), though other factors may contribute as well.

4.2 Field measurements of halogen oxides

At the inland site OLF, we measured NO_2, O_4, CHOCHO, and HCHO on a regular basis and IO on a few select days. BrO was never detected above the detection limit, likely because both NO and NO_2 readily react with BrO, forming reservoir species that can build up in the presence of high concentrations of NO_x. Hence, the instrument was moved at the end of May 2009 to the EPA site located in Gulf Breeze, FL. At the coastal EPA site, the following viewing angles from ground level with respect to the northern horizon were applied: 0.8°, 1.5°, 3.8°, 10°, 25°, 80°, 155°, 170°, 176.2°, 178.5°, and

AMTD
4, 247–284, 2011

179.2°. These measurements were applied in a fixed azimuth angle and allowed us to measure both to the north over the bay between Pensacola and Gulf Breeze and to the south over the Gulf of Mexico. Only measurements from 10 weeks at the EPA site (period from 11 March through 25 May 2010) are further discussed here.

During the spring 2010 period the instrument measured 54862 individual spectra (~4600 full sequences of elevation angles) of which 87% were recorded at SZA<80 degrees; an RMS filter (RMS<4×10^{-4}) was applied to filter outliers (8% in the HCHO spectral range, 2% in the CHOCHO spectral range). We detected significant BrO in 349 spectra (0.7%), IO in 19 998 spectra (~42%), HCHO in 31 204 spectra (~65%), CHOCHO in 15 299 spectra (~32%), NO_2 in 35 093 spectra (~74%), and O_4 in 38 433 spectra (~81%). Figures 7 and 8 show spectral proof for the measurement of these trace gases and Fig. 9 depicts a time series of the dSCDs for these trace gases from the period between 3 April and 8 April 2010. Detection limits for all observable trace gases are determined by dividing the RMS, to which a scaling factor is applied, by the absorption cross-section. The scaling factor is based on the amount of structure left in the residual, where more structure provides a basis for a higher factor and less structure, more along the lines of statistical noise, provides basis for a lower scaling factor. This factor was 2 for IO, and varied between 1.5 and 2.1 depending on elevation angle for BrO.

For IO the measured dSCDs decrease with increasing elevation angle. We conclude that IO is mostly located in the MBL. Similarly, most BrO appears to be located in the MBL, but the split in dSCD with elevation angle is less clear. Using geometric air mass factors (AMFs) to convert dSCDs from the 25° (over land) and 155° (over ocean) viewing angles to tropospheric VCDs we calculate daytime average VCDs (SZA<80°) of ~2×10^{13} molec cm^{-2} for BrO, and ~8×10^{12} molec cm^{-2} for IO. HCHO, CHOCHO and NO_2 were also observed in the MBL with daytime average VCDs of ~1×10^{16} molec cm^{-2}, ~4×10^{14} molec cm^{-2} and ~3×10^{15} molec cm^{-2}, respectively.

Field studies (Peleg et al., 2007; Lindberg et al., 2002), laboratory studies (Donohoue et al., 2006), quantum calculations (Goodsite et al., 2004; Cremer et al., 2008;

AMTD
4, 247–284, 2011

Balabanov et al., 2003; Tossell 2003), and modeling studies (Holmes et al., 2006, 2009; Selin et al., 2007) consistently suggest that a significant conversion of Hg^0 to Hg^{2+} and possibly mercury bound to particles (PHg) (Murphy et al., 2006) may be attributed to reactive halogens. Despite the growing evidence supporting the role of halogen species, to date most global mercury models still use OH and O_3 chemistry for the conversion of GEM to GOM (e.g., Bergan and Rodhe 2001; Selin et al., 2007). These models can reproduce the diurnal patterns of GOM but fail to reproduce the amplitude in GOM. This requires that they infer additional oxidants must exist. First attempts to represent bromine chemistry in models (Holmes et al., 2006) resulted in an atmospheric lifetime of GEM against conversion to GOM of 1.4 to 1.7 yr (and possibly as short as 0.5 yr), indicating that oxidation by atomic bromine would be an important and possibly dominant global pathway for oxidation and deposition of atmospheric mercury. Additionally, in a modeling study attempting to assess the potential role of bromine species in mercury oxidation, Holmes et al. (2009) found that only small amounts of bromine radicals, equivalent to <2 ppt of BrO, were needed to explain observed trends in GOM. Studies such as these provided the initial motivation for building an instrument capable of measuring halogen oxides in the marine boundary.

5 Conclusions and outlook

The accuracy of DOAS measurements of BrO and IO is RMS-limited. In order to measure such trace gases, the instrument properties and the uncertainties surrounding the DOAS retrieval were explored. We identified that the detector non-linearity of our state-of-the-art CCD detector, as well as changes in optical resolution due to small temperature variations are two key factors that can limit DOAS evaluations of solar stray-light spectra at RMS at $\sim 10^{-4}$. Both factors were addressed and minimized in the design of the CU GMAX-DOAS instrument. The instrument is able to measure RMS$<10^{-5}$ without any limitations other than photon shot noise under laboratory conditions using solar stray-light.

AMTD
4, 247–284, 2011

In a first field deployment, the CU GMAX-DOAS instrument routinely achieved RMS in the range 8×10^{-5}<RMS<3×10^{-4} and 6×10^{-5}<RMS<3×10^{-4} in the UV and visible wavelength ranges, respectively, as well as measurements of BrO, IO, CHOCHO, HCHO, NO_2, and O_4. These are the first measurements of BrO and IO over the Gulf of Mexico, providing direct evidence for the presence these halogen oxides in the MBL. BrO in the MBL indicates the availability of bromine atoms as oxidants for elemental mercury. The relevance of IO in the MBL on the observed elevated mercury wet deposition has been little studied and remains uncertain.

For a systematic characterization of the BrO vertical distribution in the MBL and FT, we propose that further RMS reduction will increase the frequency with which BrO tropospheric column amounts can be detected. However, the height resolution of a ground-based instrument is limited. For BrO located above 6 km altitude, tropospheric and stratospheric BrO become entangled, and the accuracy of tropospheric BrO measurements becomes limited by the need to make assumptions about a stratospheric BrO profile (which cannot be measured directly from ground). A solution to this quandary exists by using Airborne MAX-DOAS, since the MAX-DOAS technique is always maximally sensitive to absorbers located at or near (within a few km) the instrument altitude. However, ground based halogen oxide measurements by the CU GMAX-DOAS provide cost-effective means to infer the column abundance of halogen oxide radicals, and present constraints for the halogen atom concentration available to destroy tropospheric ozone and oxidize GEM to GOM.

Acknowledgements. The instrument was developed with support from EPRI's Technology Innovation program (EP-P27450/C13049). Additional support from EPRI (EP-P32238/C14974), NSF-CAREER (ATM-0847793) and CU Boulder startup funds is gratefully acknowledged.

AMTD
4, 247–284, 2011

References

Balabanov, N. B. and Peterson, K. A.: Mercury and reactive halogens: the thermochemistry of $Hg^{+}\{Cl_2$, Br_2, BrCl, ClO, and BrO$\}$, J. Phys. Chem. A, 107, 7465–7470, doi:10.1021/jp035547p, 2003.

Bergan, T. and Rodhe, H.: Oxidation of elemental mercury in the atmosphere; constraints imposed by global scale modelling, J. Atmos. Chem., 40, 191–212, 2001.

Bobrowski, N., Hönninger, G., Galle, B., and Platt, U.: Detection of bromine monoxide in a volcanic plume, Nature, 423, 273–276, 2003.

Bogumil, K., Orphal, J., Homann, T., Voigt, S., Spietz, P., Fleischmann, O. C., Vogel, A., Hartmann, M., Bovensmann, H., Frerick, J., and Burrows J. P.: Measurements of molecular absorption spectra with the SCIAMACHY pre-flight model: instrument characterization and reference data for atmospheric remote-sensing in the 230–2380 nm region, J. Photoch. Photobio. A, 157, 167–184, 2003.

Cremer, D., Kraka, E., and Filatov, M.: Bonding in mercury molecules described by the normalized elimination of the small component and coupled cluster theory, Chem. Phys. Chem., 9, 2510–2521, doi:10.1002/cphc.200800510, 2008.

Donohoue, D. L., Bauer, D., Cossairt, B., and Hynes, A. J.: Temperature and pressure dependent rate coefficients for the reaction of Hg with Br and the reaction of Br with Br: a pulsed laser photolysis-pulsed laser induced fluorescence study, J. Phys. Chem. A, 110, 6623–6632, doi:10.1021/jp054688j, 2006.

Fayt, C. and van Roozendael, M.: WinDoas 2.1 – Software User Manual, Brussels: BIRA-IASB, 2001.

Frieß, U., Hollwedel, J., König-Langlo, G., Wagner, T., and Platt, U.: Dynamics and chemistry of tropospheric bromine explosion events in the Antarctic coastal region, J. Geophys. Res., 109, D06305, doi:10.1029/2003JD004133, 2004.

Frieß, U., Deutschmann, T., Gilfedder, B. S., Weller, R., and Platt, U.: Iodine monoxide in the Antarctic snowpack, Atmos. Chem. Phys., 10, 2439–2456, doi:10.5194/acp-10-2439-2010, 2010.

Goodsite, M. E., Plane, J. M. C., and Skov, H.: A theoretical study of the oxidatin of Hg_0 to $HgBr_2$ in the troposphere, Environ. Sci. Technol., 38, 1772–1776, doi:10.1021/es034680s, 2004.

Hansen, D. A., Edgerton, E. S., Hartsell, B. E., Jansen, J. J., Kandasamy, N., Hidy, G. M., and

AMTD
4, 247–284, 2011

Blanchard, C. L.: The southeastern aerosol research and characterization study: Part 1 – Overview, J. Air Waste Manage., 53, 1460–1471, 2003.
Heckel, A., Richter, A., Tarsu, T., Wittrock, F., Hak, C., Pundt, I., Junkermann, W., and Burrows, J. P.: MAX-DOAS measurements of formaldehyde in the Po-Valley, Atmos. Chem. Phys., 5, 909–918, doi:10.5194/acp-5-909-2005, 2005.
Hermans, C.: Measurement of absorption cross sections and spectroscopic molecular parameters: O_2 and its collisonal induced absorption: http://spectrolab.aeronomie.be/o2.htm, 2002.
Herman, J., Cede, A., Spinei, E., Mount, G., Tzortziou, M., and Abuhassan, N.: NO_2 column amounts from ground-based Pandora and MFDOAS spectrometers using the direct-sun DOAS technique: Intercomparisons and application to OMI validation, J. Geophys. Res., 114, D13307, doi:10.1029/2009JD011848, 2009.
Holmes, C. D., Jacob, D. J., and Yang, X.: Global lifetime of elemental mercury against oxidation by atomic bromine in the free troposphere, Geophys. Res. Lett., 33, L20808, doi:10.1029/2006GL027176, 2006.
Holmes, C. D., Jacob, D. J., Mason, R. P., and Jaffe, D. A.: Sources and deposition of reactive mercury in the marine atmosphere, Atmos. Environ., 43, 2278–2285, doi:10.1016/j.atmosenv.2009.01.051, 2009.
Hönninger, G.: Referenzspektren reaktiver Halogenverbindungen für DOAS-Messungen, diploma thesis, University of Heidelberg, 1999.
Hönninger, G.: Halogen Oxide Studies in the Boundary layer by Multi Axis Differential Optical Absorption Spectroscopy and Active longpath-DOAS, Ph.D. thesis, Heidelberg of University, Germany, 2002.
Hönninger, G. and Platt, U.: Observations of BrO and its vertical distribution during surface ozone depletion at Alert, Atmos. Environ., 36, 2481–2489, 2002.
Hönninger, G., von Friedeburg, C., and Platt, U.: Multi axis differential optical absorption spectroscopy (MAX-DOAS), Atmos. Chem. Phys., 4, 231–254, doi:10.5194/acp-4-231-2004, 2004.
Ibrahim, O., Shaiganfar, R., Sinreich, R., Stein, T., Platt, U., and Wagner, T.: Car MAX-DOAS measurements around entire cities: quantification of NO_x emissions from the cities of Mannheim and Ludwigshafen (Germany), Atmos. Meas. Tech., 3, 709–721, doi:10.5194/amt-3-709-2010, 2010.
Irie, H., Kanaya, Y., Akimoto, H., Iwabuchi, H., Shimizu, A., and Aoki, K.: First retrieval of tropospheric aerosol profiles using MAX-DOAS and comparison with lidar and sky radiometer

AMTD
4, 247–284, 2011

measurements, Atmos. Chem. Phys., 8, 341–350, doi:10.5194/acp-8-341-2008, 2008.
Irie, H., Kanaya, Y., Akimoto, H., Iwabuchi, H., Shimizu, A., and Aoki, K.: Dual-wavelength aerosol vertical profile measurements by MAX-DOAS at Tsukuba, Japan, Atmos. Chem. Phys., 9, 2741–2749, doi:10.5194/acp-9-2741-2009, 2009.
Kraus, S.: DOASIS – A Framework Design for DOAS, Shaker Verlag, University of Heidelberg, Germany, 2006.
Kurucz, R. L., Furenlid, I., Brault, J., and Testerman, L.: Solar Flux Atlas from 296 to 1300 nm, Technical Report, National Solar Observatory, 1984.
Lindberg, S. E., Brooks, S., Lin, C. J., Scott, K. J., Landis, M. S., Stevens, R. K., Goodsite, M., and Richter, A.: Dynamic oxidation of gaseous mercury in the Arctic troposphere at polar sunrise, Environ. Sci. Technol., 36, 1245–1256, doi:10.1021/es011194, 2002.
Meller, R. and Moortgat, G. K.: Temperature dependence of the absorption cross sections of HCHO between 223 and 323 K in the wavelength range 225–375 nm, J. Geophys. Res., 105, 7089–7102, 2000.
Murphy, D. M., Hudson, P. K., Thomson, D. S., Sheridan, P. J., and Wilson, J. C.: Observations of mercury-containing aerosols, Environ Sci Technol, 40, 3163–3167, doi:10.1021/es052385x, 2006.
Peleg, M., Matveev, V., Tas, E., Luria, M., Valente, R. J., and Olbrist, D.: Mercury depletion events in the troposphere in mid-latitudes at the Dead Sea, Israel, Environ. Sci. Technol., 41, 7280–7285, doi:10.1021/es070320j, 2007.
Platt, U.: Differential optical absorption spectroscopy (DOAS), in: Air Monitoring by Spectroscopic Techniques, Chem. Anal. Ser., edited by: Sigrist, M. W., John Wiley & Sons, Inc., New York, 127, 1994.
Platt, U. and Perner, D.: Direct measurement of atmospheric CH_2O, HNO_2, O_3, NO_2, and SO_2 by differential optical absorption spectroscopy, J. Geophys. Res.-Oc. Atm., 85, 7453–7458, 1980.
Platt, U. and Stutz, J.: Differential Optical Absorption spectroscopy, Principles and Applications, (Physics of Earth and Space Environments), Springer, Berlin, 597, 2008.
Rothman, L. S., Jacquemart, D., Barbe, A., Benner, D. C., Birk, M., Brown, L. R., Carleer, M. R., Chackerian, C., Chance, K., Coudert, L. H., Dana, V., Devi, V. M., Flaud, J.-M., Gamache, R. R., Goldman, A., Hartmann, J.-M., Jucks, K. W., Maki, A. G., Mandin, J.-Y., Massie, S. T., Orphal, J., Perrin, A., Rinsland, C. P., Smith, M. A. H., Tennyson, J., Tolchenov, R. N., Toth, R. A., Auwera, J. V., Varanasi, P., and Wagner, G.: The HITRAN

AMTD
4, 247–284, 2011

2004 molecular spectroscopic database, J. Quant. Spectrosc. Ra., 96, 139–204, 2005.
Selin, N. E., Jacob, D. J., Park, R. J., Yantosca, R. M., Strode, S., Jaegle, L., and Jaffe, D.: Chemical cycling and deposition of atmospheric mercury: global constraints from observations, J. Geophys. Res.-Atmos., 112, D02308, doi:10.1029/2006JD007450, 2007.
Sinreich, R.: Multi-Axis Differential Optical Absorption Spectroscopy Measurements in Polluted Environments, Ph.D. thesis, University of Heidelberg, 2008.
Theys, N., Van Roozendael, M., Hendrick, F., Fayt, C., Hermans, C., Baray, J.-L., Goutail, F., Pommereau, J.-P., and De Mazière, M.: Retrieval of stratospheric and tropospheric BrO columns from multi-axis DOAS measurements at Reunion Island (21° S, 56° E), Atmos. Chem. Phys., 7, 4733–4749, doi:10.5194/acp-7-4733-2007, 2007.
Tossell, J. A.: Calculation of the energetic for oxidation of gas-phase elemental Hg by Br and BrO, J. Phys. Chem. A, 107, doi:10.1021/jp030390m, 2003.
Vandaele, A. C., Hermans, C., Simon, P. C., Carleer, M., Colin, R., Fally, S., Merienne, M.-F., Jenouvrier, A., and Coquart, B.: Measurements of the NO_2 absorption cross-section from 42 000 cm^{-1} to 10 000 cm^{-1} (238 to 1000 nm) at 220 K and 294 K, J. Quant. Spectrosc. Ra., 59, 171–184, 1997.
Vigouroux, C., Hendrick, F., Stavrakou, T., Dils, B., De Smedt, I., Hermans, C., Merlaud, A., Scolas, F., Senten, C., Vanhaelewyn, G., Fally, S., Carleer, M., Metzger, J.-M., Müller, J.-F., Van Roozendael, M., and De Mazière, M.: Ground-based FTIR and MAX-DOAS observations of formaldehyde at Réunion Island and comparisons with satellite and model data, Atmos. Chem. Phys., 9, 9523–9544, doi:10.5194/acp-9-9523-2009, 2009.
Volkamer, R., Spietz, P., Burrows, J. P., and Platt, U.: High-resolution absorption cross-section of Glyoxal in the UV/vis and IR spectral ranges, J. Photoch. Photobio. A, 172, 35–46, doi:10.1016/j.jphotochem.2004.11.011, 2005.
Volkamer, R., Coburn, S., Dix, B., and Sinreich, R.: MAX-DOAS observations from ground, ship, and research aircraft: maximizing signal-to-noise to measure "weak" absorbers, in: SPIE Proceedings "Ultraviolet and Visible Ground- and Space-based Measurements, Trace Gases, Aerosols and Effects", San Diego, 2–9 August 2009, 746203, doi:10.1117/12.826792, 2009.
Wagner, T., Ibrahim, O., Sinreich, R., Frie, U., von Glasow, R., and Platt, U.: Enhanced tropospheric BrO over Antarctic sea ice in mid winter observed by MAX-DOAS on board the research vessel Polarstern, Atmos. Chem. Phys., 7, 3129–3142, doi:10.5194/acp-7-3129-2007, 2007.

AMTD
4, 247–284, 2011

Wilmouth, D. M., Hanisco, T. F., Donahue, N. M., and Anderson, J. G.: Fourier transform ultraviolet spectroscopy of the $A^2\Pi_{3/2} \leftarrow X^2\Pi_{3/2}$ transition of BrO, J. Phys. Chem., 103, 8935–8945, 1999.

Wittrock, F., Oetjen, H., Richter, A., Fietkau, S., Medeke, T., Rozanov, A., and Burrows, J. P.: MAX-DOAS measurements of atmospheric trace gases in Ny-Ålesund – Radiative transfer studies and their application, Atmos. Chem. Phys., 4, 955–966, doi:10.5194/acp-4-955-2004, 2004.

AMTD
4, 247–284, 2011

Table 1. Summary of performance capabilities and features of some of the currently reported MAX-DOAS instruments. The notation "n.a." signifies information that was not announced.

Reference	Location	Spectrometer	Slit height/width [mm/µm]	Effective slit area [mm^2][a]	Detector make	Detector height [mm]	Optical resolution [nm]	Covered wavelength range [nm]	Temperature stability [°C]	Typical RMS
CU GMAX-DOAS[1]	Pensacola, Florida, USA/ coastal, semi-polluted	Acton SP2356i	10/110	0.6	2-dimensional CCD detector (PIXIS 400B)	8	0.77	322–488	±0.005–0.06	7×10^{-5}– 2×10^{-4}
Mini-MAX-DOAS[2]	e.g., New England, USA/ polluted	Ocean Optics USB2000	1/50	0.04	1-dimensional CCD detector (Sony ILX511)	0.014	0.7	290–420, 430–460	±0.2	8×10^{-4}
Schwampel IUP Heidelberg[2]	Mexico City/ polluted	Acton 300	10/150	0.12 (per viewing direction)	2-dimensional CCD detector (Andor DV420-OE)	6.7	0.7	325–460	±0.1	$2–4 \times 10^{-4}$
Antarctica IUP Heidelberg[3]	Antarcica/ pristine	n.a., Yobin Yvon grating	1.7/120	0.16	Photodiode array (Hamamatsu ST3904-1024)	2.5	0.5	400–650	n.a.	8.2×10^{-5}
Pandora Goddard Space Flight Center[4]	Thessaloniki, Greece, and Greenbelt, Maryland, USA	based on an Avantes spectrometer	n.a./50	0.02	1-dimensional Hamamatsu CMOS	0.025	0.42–0.52	265–500	±1	$<5 \times 10^{-3}$
MFDOAS Washington State University[4]	Greenbelt, Maryland, USA	Acton SP2356	n.a./100	0.54	2-dimensional CCD (PIXIS:2KBUV)	6.9	0.83	282--498	±2	$< 1 \times 10^{-3}$
Frontier Research Center for Global Change, Japan[5]	Tsukuba, Japan/ polluted	miniaturized UV/visible spectrometer (B&W TEK Inc., BTC111)	n.a./10	0.007	1-dimensional CCD (ILX511, Sony)	0.014	0.4–0.55	280–560	n.a.	$0.7–1.1 \times 10^{-3}$
Belgian Institute for Space Aeronomy[6]	La Reunion	Acton SpectraPro 275	n.a./n.a.	n.a.	2-dimensional CCD (NTE/CCD-400EB)	8	0.75	300–450 nm	n.a.	about 3.5×10^{-4}
IUP Bremen[7]	Ny Ålesund, Norway/ pristine	Oriel MS 257	n.a./n.a.	n.a.	2-dimensional CCD of the Andor DV 440-BU type	6.9	0.5	325–413 nm	±0.1	about 1×10^{-4}

[1] This work; [2] Hoenninger (2002a), Sinreich (2008); [3] Frieß et al. (2004, 2010); [4] Herman et al. (2009); [5] Irie et al. (2008, 2009); [6] Theys et al. (2007); Vigouroux et al. (2009); [7] Wittrock et al. (2004); Heckel et al. (2005).

[a] The effective slit area is calculated as the product of the height over which the detector is used and the slit width.

AMTD
4, 247–284, 2011

Table 2. Calculated RMS dependence on symmetric line shape broadening (Gaussian line shape).

Difference (pixels)	Range Difference (nm)	430–470 nm RMS (Dev)	330–370 nm RMS (Dev)
1	1.24E-01	1.50E-02	2.50E-02
0.1	1.24E-02	1.81E-03	3.07E-03
0.01	1.24E-03	1.84E-04	3.13E-04
0.001	1.24E-04	1.84E-05	3.14E-05
0.0001	1.24E-05	1.83E-06	3.12E-06
0.00001	1.24E-06	1.40E-07	2.38E-07

AMTD
4, 247–284, 2011

Table 3. Calculated RMS noise as a function of shift imprecision for two wavelength ranges.

Shift (pixel)	Shift (nm)	Range: 430–470 nm RMS (Dev)	Range: 430–470 nm OD Delta	Range: 330–370 nm RMS (Dev)	Range: 330–370 nm OD Delta
0.1	1.24E-02	1.69E-03	1.43E-02	2.49E-03	1.36E-02
0.01	1.24E-03	1.69E-04	1.42E-03	2.49E-04	1.37E-03
0.001	1.24E-04	1.69E-05	1.42E-04	2.49E-05	1.37E-04
0.0001	1.24E-05	1.69E-06	1.42E-05	2.49E-06	1.37E-05
0.00001	1.24E-06	1.69E-07	1.42E-06	2.49E-07	1.37E-06

AMTD
4, 247–284, 2011

Table 4. Effect of time difference between recording a measurement and "reference" spectrum on RMS.

Δ Time (s)	Median	RMS Statistics 95th Percentile	75th Percentile	25th Percentile	5th Percentile
5	7.97E-05	2.96E-04	1.26E-04	5.55E-05	4.32E-05
240	8.24E-05	2.39E-04	1.22E-04	6.03E-05	4.62E-05
900	9.49E-05	2.93E-04	1.70E-04	6.87E-05	4.83E-05
3600	1.31E-04	3.45E-04	1.99E-04	8.14E-05	5.41E-05
18 000	3.73E-04	7.10E-04	5.20E-04	2.62E-04	1.07E-04

AMTD
4, 247–284, 2011

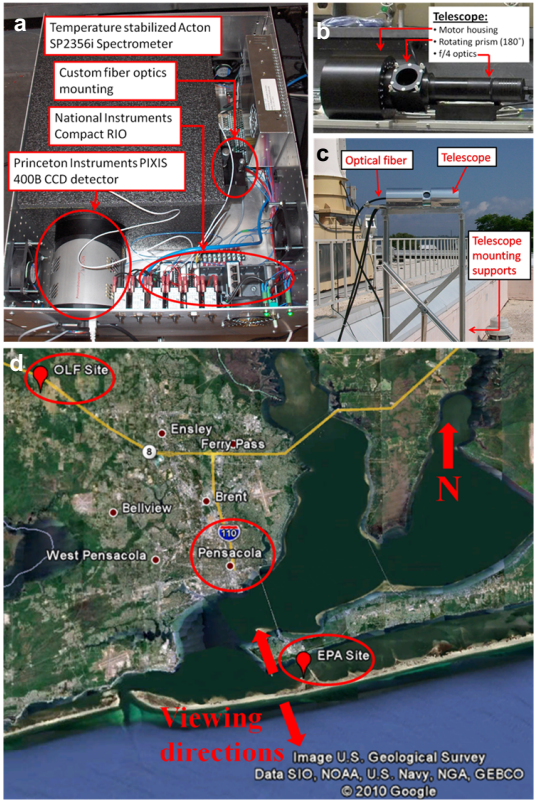

Fig. 1. Panel **(a)** Instrument rack containing ACTON2356i spectrometer, PI PIXIS400B detector, National Instruments Compact RIO with electronics modules, optical mounts to position fibers and power supplies. Panel **(b)** Telescope with housing of the MDrive34 stepper motor, rotating prism housing, and lens tube for $f/4$ optics. Panel **(c)** Outdoor setup of telescope with solar shields to reduce heating of telescope. Panel **(d)** Measurement sites: OLF located ~20 km northwest of Pensacola, FL, and EPA located in Gulf Breeze, FL~10 km southeast of Pensacola.

AMTD
4, 247–284, 2011

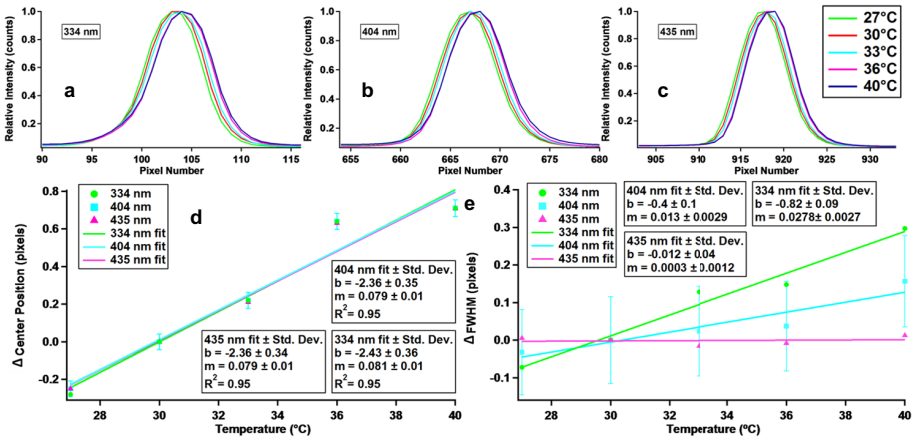

Fig. 2. Characterization of the spectrometer/detector system with respect to temperature. Panels **(a–c)** Spectral line shape as a function of temperature for 334 nm, 404 nm, and 435 nm, atomic emission lines of an Hg-Ar lamp. Panel **(d)** Spectral shift of atomic lines as a function of temperature. Panel **(e)** Difference in the full width at half the maximum of the line shapes as a function of temperature.

AMTD
4, 247–284, 2011

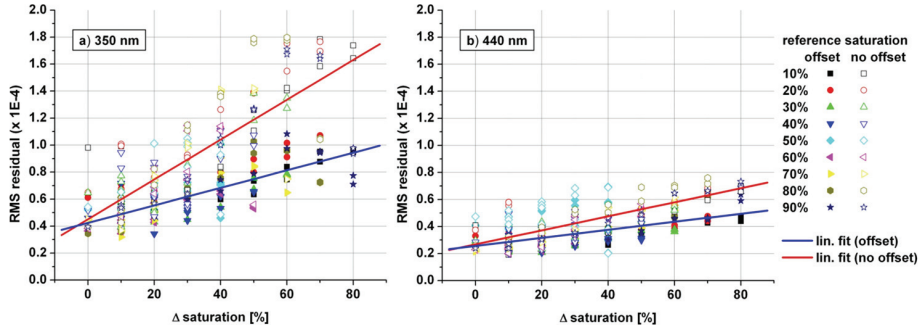

Fig. 3. Detector non-linearity expressed as the residual RMS produced from a DOAS fit at Panel **(a)** 350 nm and Panel **(b)** 440 nm as a function of the difference (sample–reference) of CCD saturation levels used to record the spectra. Open symbols represent a DOAS fit without offset spectrum, closed symbols represent a fit with offset included.

AMTD
4, 247–284, 2011

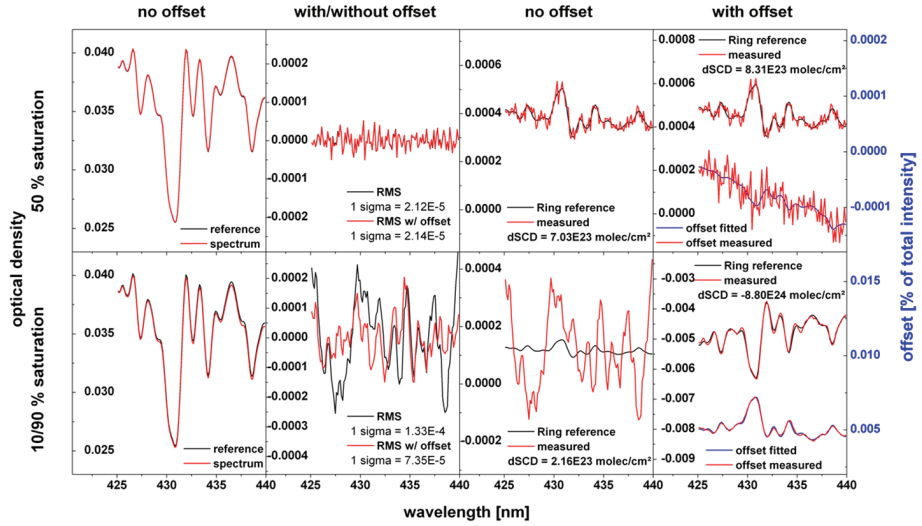

Fig. 4. Correlation of residual structures caused from incomplete elimination of Fraunhofer lines and the Ring spectrum. Two solar stray-light spectra are compared accumulating an about equal number of photons ($N=10^{10}$) by coadding of CCD acquisitions at saturation levels of 50% (upper row), and using 10% or 90% saturation level (lower row). Two fit scenarios were evaluated: (a) fit includes an "offset" and a "Ring" spectrum, (b) fit includes only the "Ring" spectrum.

AMTD
4, 247–284, 2011

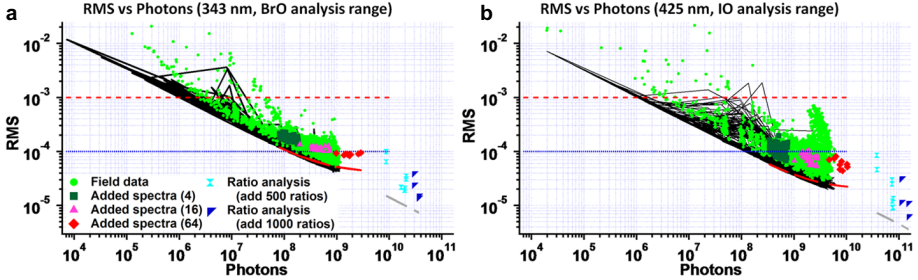

Fig. 5. Comparison of experimental and theoretical RMS noise vs. photon counting statistics for data collected between 03 March and 25 May 2010 and during July 2010. Panel **(a)** for the BrO evaluation range (340–359 nm). Panel **(b)** for the IO evaluation range (425–438 nm), except for the ratio spectra which were analyzed between 415–440 nm. Horizontal lines indicate typical RMS values of other MAX-DOAS instruments: (red dashed line) Mini-MAX-DOAS (10^{-3} RMS); (blue dotted line) research grade MAX-DOAS (10^{-4} RMS). All data depicted is for the 25° viewing angle, (green circles) field data from spring 2010; (solid black lines) represent the corresponding theoretical noise. (Dark green squares) for the July 2010 period, 4 spectra were added (without shifting) to increase the photon count, and the sum spectrum was subsequently analyzed using the WinDOAS software; (pink triangles) 16 spectra added, and (red diamonds) 64 spectra added. (Light blue hourglasses) IAM processed data taken in July 2010, where IAM created a ratio of two sequential spectra, and then added 500 of the ratios to create the final spectrum; (dark blue triangles) same for 1000 ratios.

AMTD
4, 247–284, 2011

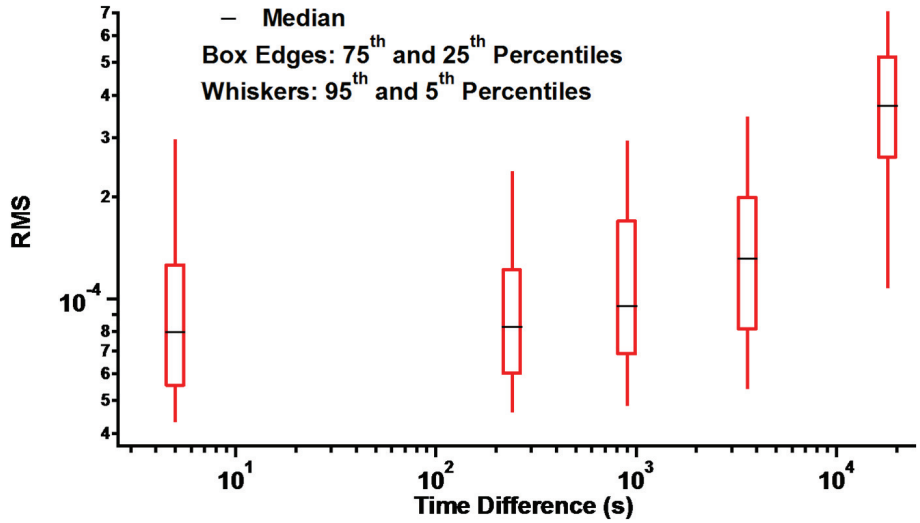

Fig. 6. RMS as a function of time difference between the spectrum analyzed and the reference. The black lines represent the median, the box edges are the 25% and 75% quartiles, and the whiskers are the 5% and 95% quartiles. In general, using a reference taken close in time to the spectrum analyzed provides better RMS values.

AMTD
4, 247–284, 2011

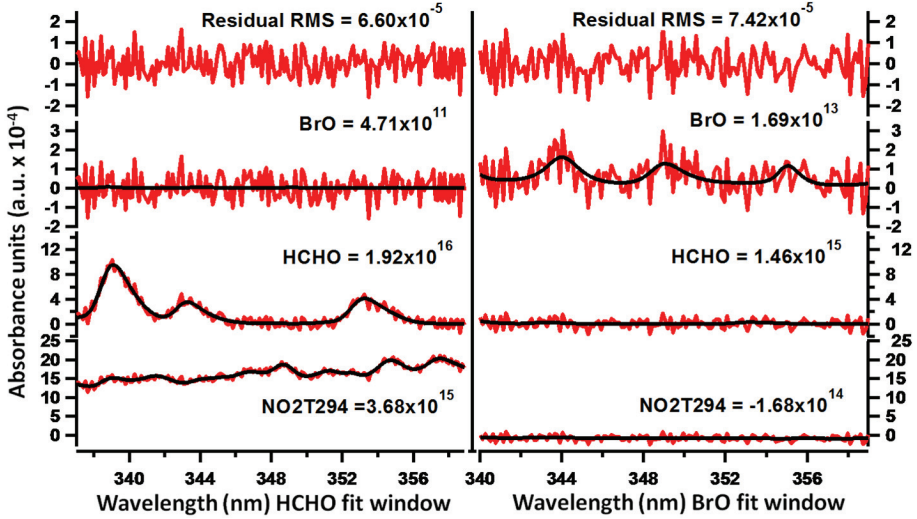

Fig. 7. Spectral proof for the detection of HCHO and BrO. All spectra were analyzed for HCHO in the 337–359 nm range and for BrO in the 340–359 nm range. The HCHO fit is from 8 May 2010 at 20:28 UTC in the 25° viewing angle, and the BrO fit is from 2 April 2010 at 19:36 UTC in the 155° viewing angle.

AMTD
4, 247–284, 2011

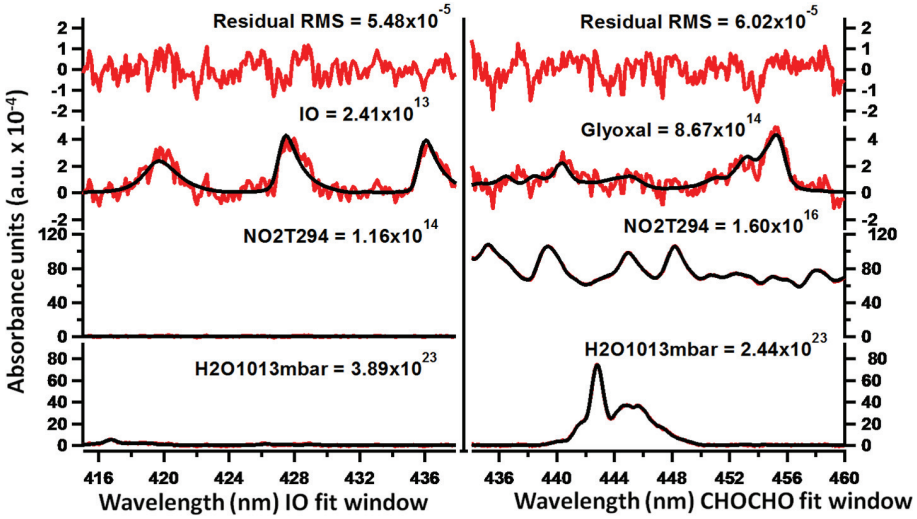

Fig. 8. Spectral proof for the detection of IO and CHOCHO. Spectra were analyzed for IO in the 425–438 nm range, while the range of 434–460 nm was used for CHOCHO. The IO fit is from 3 April 2010 at 18:42 UTC in the 179.2° viewing angle, and the CHOCHO fit is from 23 March 2010 at 19:23 UTC in the 3.8° viewing angle.

AMTD
4, 247–284, 2011

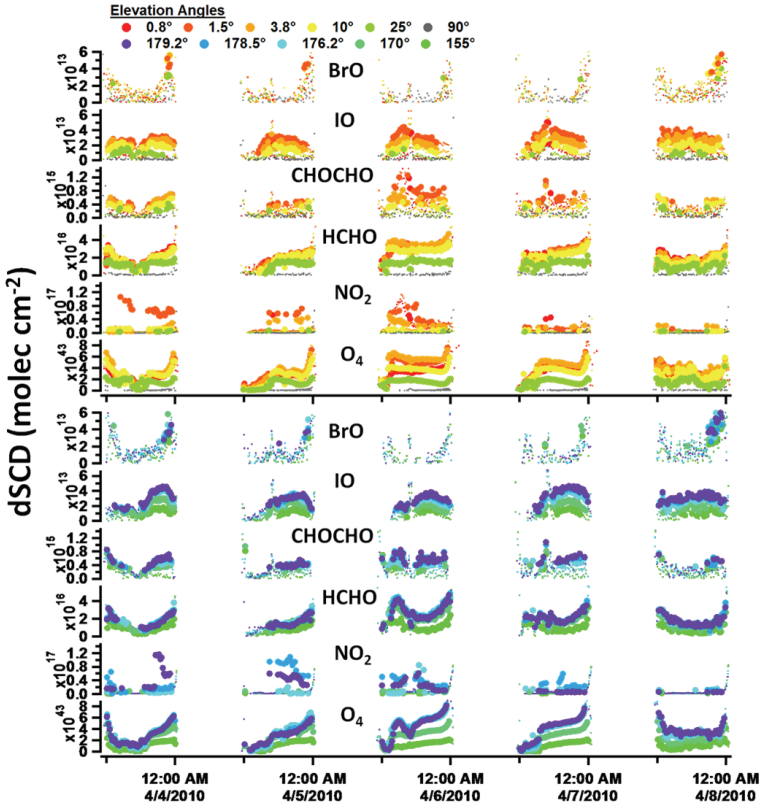

Fig. 9. Time series of the dSCDs for BrO, IO, CHOCHO, HCHO, NO_2, and O_4 between 3 April and 8 April 2010 (times are in UTC). The upper plot is for viewing directions overlooking the bay area, while the lower plot depicts the viewing directions over the open ocean. The large circles for each elevation angle represent statistically significant measurements, while the small dots are measurements that do not meet the significance criteria.

AMTD
4, 247–284, 2011